

# Ballistic Majorana nanowire devices

Önder Gül<sup>1,5\*</sup>, Hao Zhang<sup>1\*</sup>, Jouri D. S. Bommer<sup>1</sup>, Michiel W. A. de Moor<sup>1</sup>, Diana Car<sup>2</sup>, Sébastien R. Plissard<sup>2,6</sup>, Erik P. A. M. Bakkers<sup>1,2</sup>, Attila Geresdi<sup>1</sup>, Kenji Watanabe<sup>3</sup>, Takashi Taniguchi<sup>3</sup> and Leo P. Kouwenhoven<sup>1,4\*</sup>

**Majorana modes are zero-energy excitations of a topological superconductor that exhibit non-Abelian statistics<sup>1-3</sup>. Following proposals for their detection in a semiconductor nanowire coupled to an s-wave superconductor<sup>4,5</sup>, several tunnelling experiments reported characteristic Majorana signatures<sup>6-11</sup>. Reducing disorder has been a prime challenge for these experiments because disorder can mimic the zero-energy signatures of Majoranas<sup>12-16</sup>, and renders the topological properties inaccessible<sup>17-20</sup>. Here, we show characteristic Majorana signatures in InSb nanowire devices exhibiting clear ballistic transport properties. Application of a magnetic field and spatial control of carrier density using local gates generates a zero bias peak that is rigid over a large region in the parameter space of chemical potential, Zeeman energy and tunnel barrier potential. The reduction of disorder allows us to resolve separate regions in the parameter space with and without a zero bias peak, indicating topologically distinct phases. These observations are consistent with the Majorana theory in a ballistic system<sup>21</sup>, and exclude the known alternative explanations that invoke disorder<sup>12-16</sup> or a nonuniform chemical potential<sup>22,23</sup>.**

Semiconductor nanowires are the primary contender for realizing a topological quantum bit (qubit) based on Majorana modes. Their confined geometry together with highly tunable electronic properties readily allow for localizing Majoranas, engineering the coupling between Majoranas and controlling the coupling between the topological superconductor and the external circuitry. These requirements for the implementation of a Majorana qubit are challenging to achieve in other Majorana systems such as 2D and 3D topological insulators. Moreover, various basic networks<sup>24</sup> and high-quality interfaces to different superconductors<sup>18-20</sup> have already been realized in semiconductor nanowires, fulfilling the further requirements for Majorana qubits. However, despite these advances in materials, alternative explanations have been proposed for the characteristic Majorana signatures. Most alternative explanations invoke bulk or interface disorder<sup>12-16</sup> or a nonuniform chemical potential along the wire<sup>22,23</sup>. Notable examples are weak antilocalization<sup>14</sup>, Kondo effect<sup>15</sup> and Andreev levels<sup>16,22</sup>, all shown to result in transport signatures mimicking those attributed to Majoranas. Here, we show characteristic Majorana signatures in nanowire devices that exhibit ballistic transport, ruling out all known disorder- or nonuniformity-based explanations.

Figure 1a shows the measured device consisting of an InSb nanowire (green) contacted with a grounded NbTiN

superconductor (purple) and normal metal leads (yellow). The local bottom gate electrodes are separated from the nanowire by a boron nitride flake and are operated individually to allow for spatial control of the carrier density in the nanowire. We have realized our devices following our recently developed nanofabrication recipe which results in a high-quality InSb–NbTiN interface, an induced hard superconducting gap, and ballistic transport in the proximitized nanowire (see refs<sup>19,20</sup>). All measurements are performed in a dilution refrigerator with an electron temperature of ~50 mK. The data is taken by applying a bias voltage,  $V$ , between the normal metal lead and the superconductor indicated by N and S, respectively, and monitoring the current flow. The other normal lead is kept floating.

Figure 1b shows the differential conductance  $dI/dV$  while varying  $V$ , and stepping the voltage applied to the barrier gate. Importantly, we find no signs of formation of quantum dots or any other localization effects. Vertical line cuts at the gate voltages indicated with coloured bars are shown in Fig. 1c. Figure 1c (bottom) is from the tunnelling regime of the device where a sufficiently negative voltage on the barrier gate locally depletes the noncovered nanowire section, and creates a tunnel barrier between the normal lead and the superconductor. In this regime we find an induced superconducting gap with a strong conductance suppression for subgap bias. The extracted gap value is  $\Delta^* = 0.65$  meV. Increasing the voltage on the barrier gate first lowers the tunnel barrier and then removes it completely. Figure 1c (top) is from the regime in which the noncovered nanowire section admits a single fully transmitting transport channel. In this regime the subgap conductance is strongly enhanced due to Andreev reflection compared to the large-bias (above-gap) conductance of  $2e^2/h$ , the conductance quantum, where  $e$  is the elementary charge and  $h$  is the Planck constant. The extracted enhancement factor  $> 1.5$  implies a contact interface transparency  $> 0.93$  (ref.<sup>20</sup>). Figure 1d shows the horizontal line cuts from Fig. 1b at the bias voltages indicated with coloured bars. For a bias  $V > \Delta^*$  we find a quantized conductance plateau at  $2e^2/h$ , a clear signature of a ballistic device. For zero bias voltage the strong Andreev enhancement is evident in the plateau region followed by a dip in conductance due to channel mixing<sup>20</sup>. From the absence of quantum dots, the observed induced gap with a strongly reduced subgap density of states, high interface transparency, and quantized conductance, we conclude a very low disorder strength for our device, consistent with our recent findings<sup>20</sup>.

We now turn to the tunnelling regime of the device where Majorana modes are characterized by a zero bias peak. To drive the nanowire device into the topological phase, we apply a magnetic

<sup>1</sup>QuTech and Kavli Institute of Nanoscience, Delft University of Technology, Delft, The Netherlands. <sup>2</sup>Department of Applied Physics, Eindhoven University of Technology, Eindhoven, The Netherlands. <sup>3</sup>Advanced Materials Laboratory, National Institute for Materials Science, Tsukuba, Japan. <sup>4</sup>Microsoft Station Q Delft, Delft, The Netherlands. Present addresses: <sup>5</sup>Department of Physics, Harvard University, Cambridge, MA, USA. <sup>6</sup>CNRS-Laboratoire d'Analyse et d'Architecture des Systèmes (LAAS), Université de Toulouse, Toulouse, France. Önder Gül, Hao Zhang and Jouri D. S. Bommer contributed equally to this work. \*e-mail: [onder\\_gul@g.harvard.edu](mailto:onder_gul@g.harvard.edu); [h.zhang-3@tudelft.nl](mailto:h.zhang-3@tudelft.nl); [l.p.kouwenhoven@tudelft.nl](mailto:l.p.kouwenhoven@tudelft.nl)

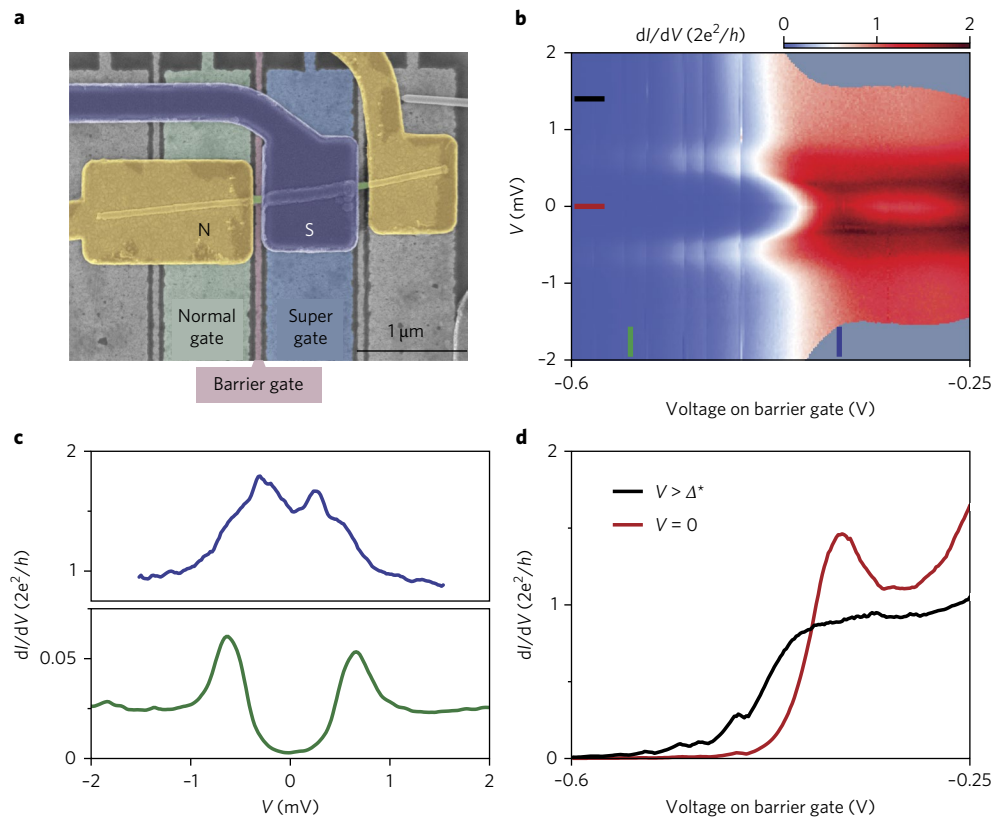


**Fig. 1 | Hybrid device and ballistic transport properties.** **a**, False-colour electron micrograph of the measured device. The InSb nanowire (green) is contacted by a grounded NbTiN superconductor (purple) and two Au normal metal leads (yellow). The nanowire has a diameter of  $\sim 80$  nm. The local bottom gates (normal, barrier and super) are separated from the nanowire by a boron nitride flake ( $\sim 30$  nm) and are operated individually. Two-terminal measurements are performed between N and S, while the other normal lead is floating. **b**, Differential conductance  $dI/dV$  as a function of bias voltage  $V$ , and voltage on the barrier gate (the other gate electrodes are grounded). Vertical lines at certain gate voltages are due to slow fluctuations in the electrostatic environment. **c**, Vertical line cuts from **b** at the gate voltages marked with coloured bars. Top panel, the  $dI/dV$  from the transport regime in which the current is carried by a single fully transmitting channel. We find an enhancement of conductance at small bias by more than a factor of 1.5 compared to the large-bias conductance of  $2e^2/h$ . Bottom panel, the tunnelling regime in which the current is carried by a single channel with low transmission. We extract an induced superconducting gap  $\Delta^* = 0.65$  meV. **d**, Horizontal line cuts from **b** at the bias voltages marked with coloured bars. Subgap conductance ( $V = 0$ ) shows an enhancement reaching  $1.5 \times 2e^2/h$  when the large-bias conductance ( $V = 1.4$  mV  $> \Delta^*$ ) has a quantized value of  $2e^2/h$ .

field,  $B$ , along the wire axis and tune the voltage applied to the super gate ( $V_{s\text{-gate}}$ ) which controls  $\mu$ , the chemical potential in the nanowire section underneath the superconductor. Figure 2a shows that an increasing  $B$  closes the induced gap at 0.55 T and generates a zero bias peak rigidly bound to  $V = 0$  up to 1.2 T (line cuts in Supplementary Fig. 1a). The gap closure is expected to occur for a Zeeman energy  $E_z > \sim \Delta^*$ . From linear interpolation we find  $g > \sim 40$  which matches our independent measurements<sup>25,26</sup>. Converting the  $B$  axis into a Zeeman energy ( $E_z$ ) scale (right vertical axis), we find that the zero bias peak is bound to zero over 0.75 meV, a range in Zeeman energy that is 30 times larger than the peak width (the full width at half maximum, FWHM  $\sim 20$   $\mu$ eV, see Supplementary Figs. 1c and 4). This excludes a level crossing as the origin for our zero bias peak<sup>15</sup>. We note that all our devices show a significant increase of subgap density of states for the magnetic fields required for topological phase transition. This behaviour is likely due to vortex formation or a short mean free path<sup>27,28</sup> in our NbTiN film. The formation of vortices is speculated to create a dissipation channel<sup>21</sup>, the leading hypothetical mechanism that limits our zero bias peak height from reaching the quantized value of  $2e^2/h$ . We have recently observed a quantized zero bias conductance in InSb nanowires proximitized by aluminium grown epitaxially on the wire<sup>29</sup>.

The origin of the zero bias peak can be spatially resolved by varying the voltages applied to individual gates. Figure 2b shows that

the presence of the zero bias peak is not affected when gating the wire section underneath the normal contact, which changes the conductance by more than a factor of five (see also Supplementary Fig. 1d). Extending the same analysis to the noncovered wire section yields the same result (Fig. 2c), that is, changing the tunnel barrier conductance by nearly an order of magnitude does not split the zero bias peak, nor makes it disappear (see also Supplementary Fig. 1e). In contrast, Fig. 2d shows that the zero bias peak is present over a finite range in voltage applied to the super gate (line cuts in Supplementary Fig. 1f). This indicates that proper tuning of  $\mu$  is essential for the appearance of the zero bias peak. The observation of a zero bias peak that does not split when changing the tunnel barrier conductance (Fig. 2c) excludes the Kondo effect<sup>15</sup> and crossing of Andreev levels<sup>16</sup> as the origin of our zero bias peak. Most importantly, it rules out an explanation provided by recent theoretical work<sup>22</sup> that demonstrated trivial Andreev levels localized near the noncovered wire section that are bound to zero energy for varying  $E_z$  and  $\mu$ , but quickly split to finite energies for varying tunnel barrier strength (see also Supplementary Text 1). Here we demonstrate a zero bias peak rigidly bound to  $V = 0$  over a changing tunnel barrier conductance—a behaviour observed in all devices (Supplementary Figs. 5–7). From the combined analysis (Fig. 2b–d) we conclude that the zero bias peak originates in the wire section underneath the superconductor, consistent with a Majorana interpretation.

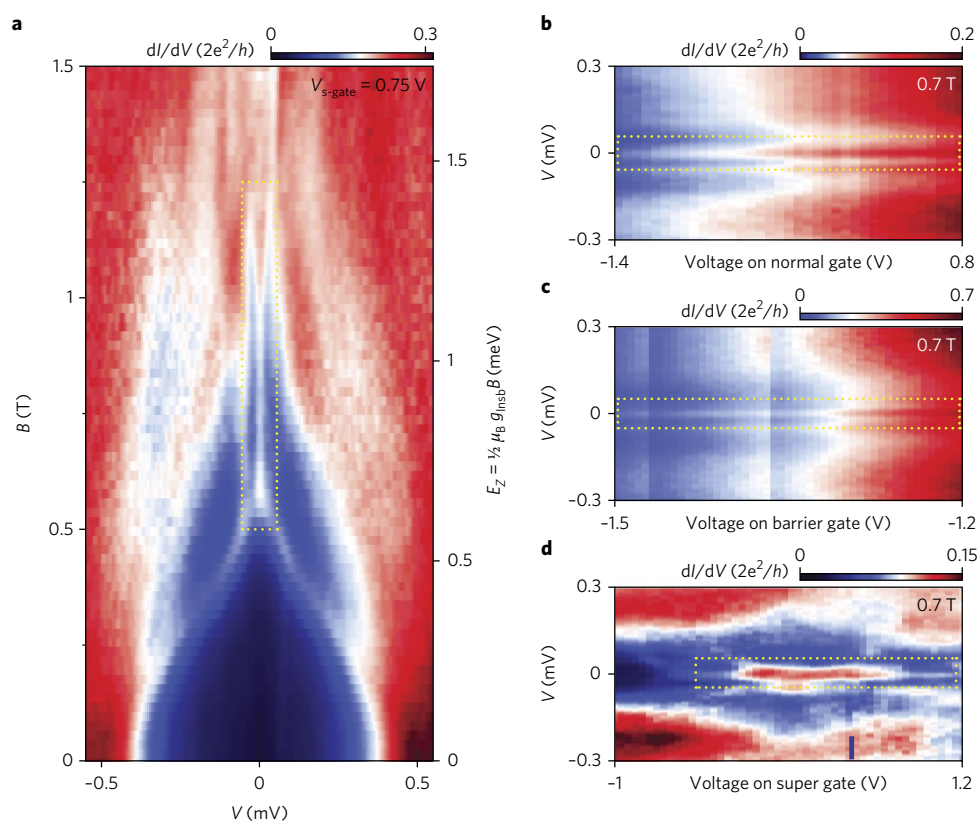


**Fig. 2 | Zero bias peak and its dependence on magnetic field and local gate voltages.** **a**, Differential conductance ( $dI/dV$ ) as a function of bias voltage ( $V$ ), and an external magnetic field ( $B$ ) along the nanowire axis for  $V_{s\text{-gate}} = 0.75$  V. The magnetic field closes the induced gap at 0.55 T and generates a zero bias peak which persists up to 1.2 T. The right axis scales with Zeeman energy ( $E_z$ ) assuming a  $g$  factor of 40 obtained independently<sup>25,26</sup>. (Voltage on the normal and barrier gate: 0 V and  $-1.4$  V.) **b**,  $dI/dV$  as a function of  $V$  and voltage on the normal gate. The voltage on the normal gate changes the conductance by more than a factor of five but does not affect the presence of the zero bias peak. **c**,  $dI/dV$  as a function of  $V$  and voltage on the barrier gate. The voltage on the barrier gate changes the conductance by nearly an order of magnitude but does not affect the presence of the zero bias peak. **d**,  $dI/dV$  as a function of  $V$  and voltage on super gate. The zero bias peak persists for a finite gate voltage range. The blue bar indicates the voltage on the super gate in **a**, **b** and **c**. The voltage on the barrier gate is adjusted to keep the overall conductance the same when sweeping the voltage on the super gate.

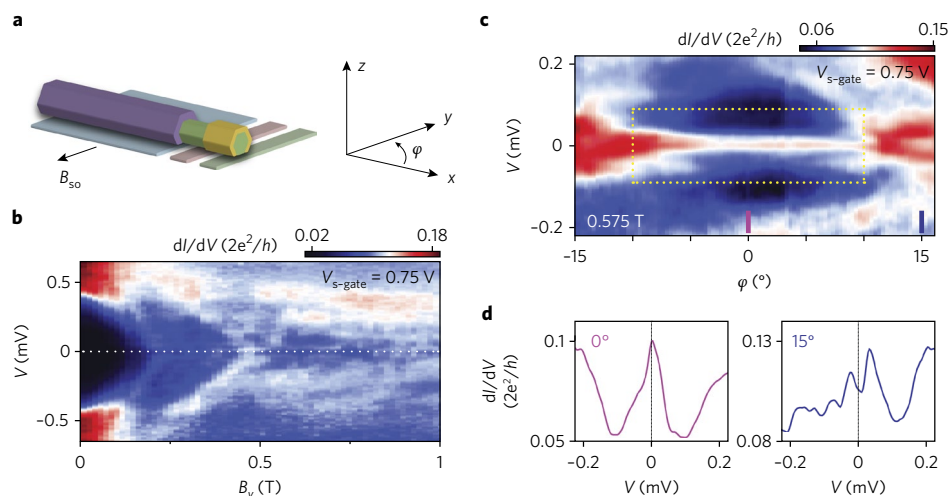


**Fig. 3 | Dependence of zero bias peak on magnetic field orientation.** **a**, Orientation of the nanowire device. The wire is along  $x$  and the spin-orbit field  $B_{so}$  is along  $y$ . The substrate plane is spanned by  $x$  and  $y$ .  $\phi$  is the angle between the  $x$ -axis and the orientation of the external magnetic field in the plane of the substrate. **b**, Differential conductance ( $dI/dV$ ) as a function of bias voltage ( $V$ ), and an external magnetic field along the  $y$ -axis. Application of a magnetic field along  $B_{so}$  closes the induced gap but does not generate a zero bias peak. **c**,  $dI/dV$  as a function of  $V$ , and in-plane rotation of the magnetic field with a magnitude of 0.575 T. The zero bias peak appears in an angle range in which the external magnetic field is mostly aligned with the wire. We attribute the low conductance region around the zero bias peak to the induced gap. Orienting the magnetic field away from the wire axis and more towards  $B_{so}$  closes the induced gap and splits the zero bias peak (see line cuts in **d**). **d**, Vertical line cuts from **c** at the angles indicated with coloured bars. For  $\phi = 0^\circ$  the zero bias peak is present, which is split for  $\phi = 15^\circ$ .

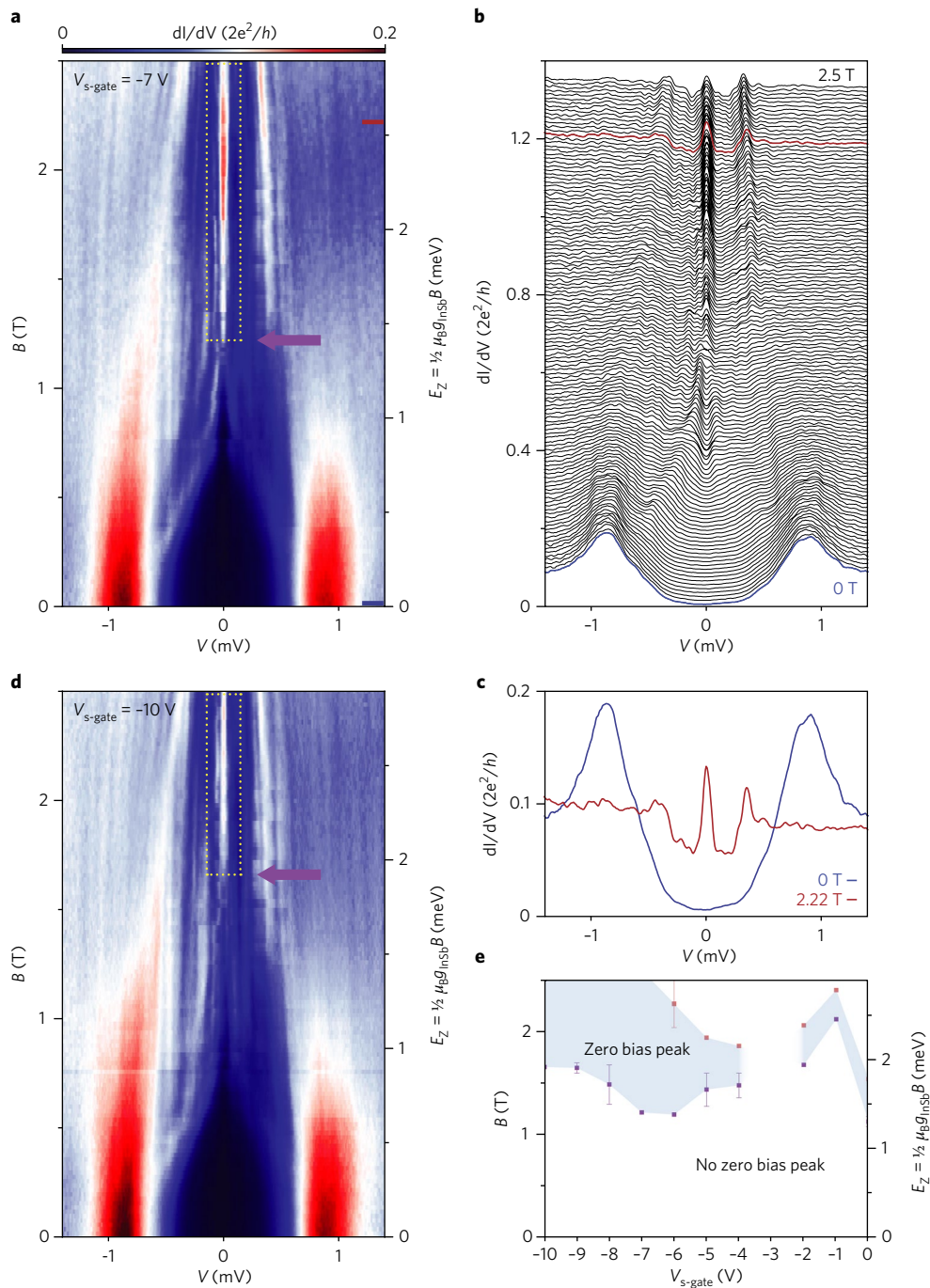


**Fig. 4 | Zero bias peak and phase diagram.** **a**, Differential conductance ( $dI/dV$ ) of another device measured as a function of bias voltage ( $V$ ), and an external magnetic field ( $B$ ) along the nanowire axis. We find an induced gap  $\Delta^* = 0.9$  meV at zero magnetic field. Increasing the magnetic field closes the induced gap at  $\sim 1$  T and generates a zero bias peak that persists up to at least 2.5 T. The right axis scales with Zeeman energy ( $E_z$ ), assuming  $g_{\text{InSb}} = 40$  obtained independently<sup>25,26</sup>. The purple arrow at 1.22 T indicates the onset of the zero bias peak. **b**, Line cuts from **a** with  $0.01 \times 2e^2/h$  offset. **c**, Line cuts from **a** and **b** at 0 and 2.22 T. **d**, Same as **a** but with a different super gate voltage  $V_{s\text{-gate}} = -10$  V. For this super gate voltage, the onset of the zero bias peak is at a larger magnetic field of 1.66 T, as marked by a purple arrow. **e**, Phase diagram constructed by the onset and the end of the zero bias peak in magnetic field for different super gate voltages. The purple squares denote the onset, pink the end. For  $V_{s\text{-gate}} = -3$  V no zero bias peak is observed.

In a Majorana nanowire<sup>4,5</sup>, the existence of a topological phase strictly requires an external magnetic field with a finite component perpendicular to the spin-orbit field  $B_{\text{SO}}$ , see Fig. 3a. An external field along the wire fulfills this requirement, shown in Fig. 2a. In contrast, Fig. 3b shows that an external magnetic field parallel to  $B_{\text{SO}}$  does not generate a zero bias peak for the same gate settings as in Fig. 2a. Figure 3c shows the dependence of the zero bias peak on

the direction of the external field. The zero bias peak is limited to an angle range where the external field is mostly aligned with the wire, perpendicular to  $B_{\text{SO}}$  (see Supplementary Fig. 2 for a measurement in a larger angle range). We observe a low conductance region around the zero bias peak, indicating the induced gap. Orienting the magnetic field away from the wire axis and more towards  $B_{\text{SO}}$  closes the induced gap and splits the zero bias peak. This is indicated by

the vertical line cuts from Fig. 3c at marked angles, shown in Fig. 3d. A gap closing is expected for the critical angle  $\phi_c$  given by the projection rule<sup>30,31</sup>  $E_c \sin(\phi_c) = \Delta^*$ . From the observed gap  $\Delta^* = 175 \mu\text{eV}$  at  $B = 0.575 \text{ T}$  and a  $g$ -factor of 40, we obtain  $\phi_c = 15^\circ$ , agreeing well with the observed value of  $\phi_c \sim 10^\circ$  (a reduction in  $\phi_c$  is expected due to the orbital effect of the external magnetic field<sup>32</sup>). Finally, in Supplementary Fig. 2 we show that increasing  $B$  decreases  $\phi_c$ , a behaviour consistent with the projection rule.

We now turn our attention to an identical device but with a longer proximitized wire section (1.2  $\mu\text{m}$ , see Supplementary Fig. 3a). Figure 4a–c shows an induced gap  $\Delta^* = 0.9 \text{ meV}$  at zero magnetic field, significantly larger than the device in Figs. 1–3. As a result, the induced gap closes at a higher magnetic field ( $\sim 1 \text{ T}$ ). The zero bias peak is visible and unsplit over a range of at least 1.3 T, corresponding to a Zeeman energy scale  $> 1.5 \text{ meV}$ . The FWHM is around 0.07 meV yielding a ratio ZBP-range/FWHM  $\gtrsim 20$  (Supplementary Fig. 4). A disorder-free Majorana theory model with parameters extracted from this device (geometry, induced gap, spin–orbit coupling, temperature) finds perfect agreement between simulation<sup>21</sup> and our data (Fig. 4a). Supplementary Fig. 3b,c shows that the zero bias peak position is robust against a change in conductance when varying the voltage applied to the normal and the barrier gate, ruling out the trivial Andreev-level explanation<sup>22</sup> consistent with our earlier discussion (Fig. 2b,c). In contrast to normal and barrier gate, the voltage applied to the super gate changes the onset and the end of the zero bias peak in magnetic field. Figure 4d shows that for  $V_{\text{s-gate}} = -10 \text{ V}$  the zero bias peak appears at a higher magnetic field compared to Fig. 4a where  $V_{\text{s-gate}} = -7 \text{ V}$  (1.66 T versus 1.22 T). We have extended this analysis for  $-10 \text{ V} \leq V_{\text{s-gate}} \leq 0 \text{ V}$  and marked the magnetic field values at which the zero bias peak starts and ends (Supplementary Fig. 3d). The resulting phase diagram is shown in Fig. 4e. For large negative voltages applied to the super gate, we find a region in which the zero bias peak persists for large ranges of magnetic field and  $V_{\text{s-gate}}$ , indicating the topological phase. We attribute the appearance of a trivial phase at large magnetic fields above the topological phase to multi-channel occupation in the proximitized wire section<sup>21,22</sup>. A precise knowledge of the phase boundaries requires a theory including finite-size effects<sup>33</sup>, the orbital effect of the magnetic field<sup>32</sup> and accurate electrostatic modelling of the device<sup>34</sup>, and will be addressed in future studies.

In conclusion, the presented experiments demonstrate zero bias peaks over an extended range in Zeeman energy and gate voltage in devices that show clear ballistic transport properties, and reveal the distinct phases in the topology of Majorana wires. These observations exclude all known alternative explanations for our zero bias peaks that are based on disorder.

## Methods

Methods, including statements of data availability and any associated accession codes and references, are available at <https://doi.org/10.1038/s41565-017-0032-8>.

Received: 15 June 2017; Accepted: 20 November 2017;

Published online: 15 January 2018

## References

- Read, N. & Green, D. Paired states of fermions in two dimensions with breaking of parity and time-reversal symmetries and the fractional quantum Hall effect. *Phys. Rev. B* **61**, 10267 (2000).
- Kitaev, A. Y. Unpaired Majorana fermions in quantum wires. *Phys. Usp.* **44**, 131–136 (2001).
- Fu, L. & Kane, C. L. Superconducting proximity effect and Majorana fermions at the surface of a topological insulator. *Phys. Rev. Lett.* **100**, 096407 (2008).
- Lutchyn, R. M., Sau, J. D. & Das Sarma, S. Majorana fermions and a topological phase transition in semiconductor–superconductor heterostructures. *Phys. Rev. Lett.* **105**, 077001 (2010).
- Oreg, Y., Refael, G. & von Oppen, F. Helical liquids and Majorana bound states in quantum wires. *Phys. Rev. Lett.* **105**, 177002 (2010).
- Mourik, V. et al. Signatures of Majorana fermions in hybrid superconductor–semiconductor nanowire devices. *Science* **336**, 1003–1007 (2012).
- Das, A. et al. Zero-bias peaks and splitting in an Al–InAs nanowire topological superconductor as a signature of Majorana fermions. *Nat. Phys.* **8**, 887–895 (2012).
- Deng, M. T. et al. Anomalous zero-bias conductance peak in a Nb–InSb nanowire–Nb hybrid device. *Nano Lett.* **12**, 6414–6419 (2012).
- Albrecht, S. M. et al. Exponential protection of zero modes in Majorana islands. *Nature* **531**, 206–209 (2016).
- Deng, M. T. et al. Majorana bound state in a coupled quantum-dot hybrid-nanowire system. *Science* **354**, 1557–1562 (2016).
- Chen, J. et al. Experimental phase diagram of zero-bias conductance peaks in superconductor/semiconductor nanowire devices. *Sci. Adv.* **3**, e1701476 (2017).
- Liu, J., Potter, A. C., Law, K. T. & Lee, P. A. Zero-bias peaks in the tunneling conductance of spin-orbit-coupled superconducting wires with and without Majorana end-states. *Phys. Rev. Lett.* **109**, 267002 (2012).
- Bagrets, D. & Altland, A. Class D spectral peak in Majorana quantum wires. *Phys. Rev. Lett.* **109**, 227005 (2012).
- Pikulin, D. I., Dahlhaus, J. P., Wimmer, M., Schomerus, H. & Beenakker, C. W. J. A zero-voltage conductance peak from weak antilocalization in a Majorana nanowire. *New J. Phys.* **14**, 125011 (2012).
- Lee, E. J. H. et al. Zero-bias anomaly in a nanowire quantum dot coupled to superconductors. *Phys. Rev. Lett.* **109**, 186802 (2012).
- Lee, E. J. H. et al. Spin-resolved Andreev levels and parity crossings in hybrid superconductor–semiconductor nanostructures. *Nat. Nanotech.* **9**, 79–84 (2014).
- Takei, S., Fregoso, B. M., Hui, H.-Y., Lobos, A. M. & Das Sarma, S. Soft superconducting gap in semiconductor Majorana nanowires. *Phys. Rev. Lett.* **110**, 186803 (2013).
- Chang, W. et al. Hard gap in epitaxial semiconductor–superconductor nanowires. *Nat. Nanotech.* **10**, 232–236 (2015).
- Gül, Ö. et al. Hard superconducting gap in InSb nanowires. *Nano Lett.* **17**, 2690–2696 (2017).
- Zhang, H. et al. Ballistic superconductivity in semiconductor nanowires. *Nat. Commun.* **8**, 16025 (2017).
- Liu, C.-X., Sau, J. D. & Das Sarma, S. Role of dissipation in realistic Majorana nanowires. *Phys. Rev. B* **95**, 054502 (2017).
- Liu, C.-X., Sau, J. D., Stanescu, T. D. & Das Sarma, S. Andreev bound states versus Majorana bound states in quantum dot–nanowire–superconductor hybrid structures: trivial versus topological zero-bias conductance peaks. *Phys. Rev. B* **96**, 075161 (2017).
- Prada, E., San-Jose, P. & Aguado, R. Transport spectroscopy of NS nanowire junctions with Majorana fermions. *Phys. Rev. B* **86**, 180503(R) (2012).
- Gazibegovic, S. et al. Epitaxy of advanced nanowire quantum devices. *Nature* **548**, 434–438 (2017).
- Kammhuber, J. et al. Conductance quantization at zero magnetic field in InSb nanowires. *Nano Lett.* **16**, 3482–3486 (2016).
- Kammhuber, J. et al. Conductance through a helical state in an indium antimonide nanowire. *Nat. Commun.* **8**, 478 (2017).
- Cole, W. S., Sau, J. D. & Das Sarma, S. Proximity effect and Majorana bound states in clean semiconductor nanowires coupled to disordered superconductors. *Phys. Rev. B* **94**, 150505(R) (2017).
- Stanescu, T. D. & Das Sarma, S. Proximity-induced low-energy renormalization in hybrid semiconductor–superconductor Majorana structures. *Phys. Rev. B* **96**, 014510 (2017).
- Zhang, H. et al. Quantized Majorana conductance. Preprint at <https://arxiv.org/abs/1710.10701> (2017).
- Osca, J., Ruiz, D. & Serra, L. Effects of tilting the magnetic field in one-dimensional Majorana nanowires. *Phys. Rev. B* **89**, 245405 (2014).
- Rex, S. & Sudbø, A. Tilting of the magnetic field in Majorana nanowires: critical angle and zero-energy differential conductance. *Phys. Rev. B* **90**, 115429 (2014).
- Nijholt, B. & Akhmerov, A. R. Orbital effect of magnetic field on the Majorana phase diagram. *Phys. Rev. B* **93**, 235434 (2016).
- Mishmash, R. V., Aasen, D., Higginbotham, A. P. & Alicea, J. Approaching a topological phase transition in Majorana nanowires. *Phys. Rev. B* **93**, 245404 (2016).
- Vuik, A., Eeltink, D., Akhmerov, A. R. & Wimmer, M. Effects of the electrostatic environment on the Majorana nanowire devices. *New J. Phys.* **18**, 033013 (2016).

## Acknowledgements

We thank A. R. Akhmerov, O. W. B. Benningshof, M. C. Cassidy, S. Goswami, J. Kammhuber, V. Mourik, M. Quintero-Pérez, J. Shen, M. Wimmer, D. J. van Woerkom and K. Zuo for discussions and assistance. This work has been supported by the Netherlands Organisation for Scientific Research (NWO), European Research Council (ERC) and Microsoft Corporation Station Q.

**Author contributions**

Ö.G., H.Z. and J.D.S.B fabricated the devices, performed the measurements, and analysed the data. M.W.A.d.M. contributed to the device fabrication. D.C., S.P. and E.P.A.M.B. grew the InSb nanowires. A.G. contributed to the experiments. K.W. and T.T. synthesized the hBN crystals. L.P.K. supervised the project. Ö.G., H.Z. and J.D.S.B. co-wrote the paper. All authors commented on the manuscript.

**Competing interests**

The authors declare no competing financial interests.

**Additional information**

**Supplementary information** is available for this paper at <https://doi.org/10.1038/s41565-017-0032-8>.

**Reprints and permissions information** is available at [www.nature.com/reprints](http://www.nature.com/reprints).

**Correspondence and requests for materials** should be addressed to Ö.G. or H.Z. or L.P.K.

**Publisher's note:** Springer Nature remains neutral with regard to jurisdictional claims in published maps and institutional affiliations.

## Methods

**Nanowire growth and device fabrication.** InSb nanowires are grown by a Au-catalysed vapour–liquid–solid mechanism in a metal organic vapour phase epitaxy reactor. The InSb nanowires are zinc blende, along the [111] crystal direction, and are free of stacking faults and dislocations<sup>35</sup>. As-grown nanowires are deposited one-by-one using a micro-manipulator<sup>36</sup> on a substrate patterned with local gates covered by a ~30-nm-thick hBN dielectric. The contact deposition process starts with resist development followed by oxygen plasma cleaning. Then, the chip is immersed in a sulfur-rich ammonium sulfide solution diluted by water (at a ratio of 1:200) at 60°C for half an hour<sup>37</sup>. At all stages care is taken to expose the solution to as little air as possible. For normal metal contacts<sup>25,26</sup>, the chip is placed into an evaporator. 30 seconds of helium ion milling is performed in situ before evaporation of Cr/Au (10 nm/125 nm) at a base pressure < 10<sup>-7</sup> mbar. For superconducting contacts<sup>19,20</sup>, the chip is mounted in a sputtering system. After 5 seconds of in-situ argon plasma etching at a power of 25 watts and a pressure of 10 mTorr, 5 nm NbTi is sputtered followed by 85 nm NbTiN.

**Data availability.** All data are available at <http://doi.org/10.4121/uuid:b3f993a7-1b8b-4fd8-8142-5fa577027cdd> (ref. <sup>38</sup>).

## References

35. Car, D., Wang, J., Verheijen, M. A., Bakkers, E. P. A. M. & Plissard, S. R. Rationally designed single-crystalline nanowire networks. *Adv. Mater.* **26**, 4875–4879 (2014).
36. Flöhr, K. et al. Manipulating InAs nanowires with submicrometer precision. *Rev. Sci. Instrum.* **82**, 113705 (2011).
37. Suyatin, D. B., Thelander, C., Björk, M. T., Maximov, I. & Samuelson, L. Sulfur passivation for ohmic contact formation to InAs nanowires. *Nanotechnology* **18**, 105307 (2007).
38. Gül, Ö. et al. Ballistic Majorana nanowire devices. 4TU.ResearchData. <https://doi.org/10.4121/uuid:b3f993a7-1b8b-4fd8-8142-5fa577027cdd> (2017).